

1 Microstructural Changes in White Portland Cement Paste Under the First Drying Process Evaluated by WAXS, SAXS, and
2 USAXS

3
4 Ippei Maruyama^{1)*}, Naoki Sakamoto²⁾, Kunio Matsui³⁾, and Go Igarashi⁴⁾

5
6 1) Associate Professor, Ph.D., Graduate School of Environmental Studies, Nagoya University
7 ES Building, No. 546, Furo-cho, Chikusa-ku, Nagoya, Aichi 464-8603, Japan

8 *Corresponding author:

9 E-mail: ippei@dali.nuac.nagoya-u.ac.jp

10 Tel: +81-52-789-3761, Fax: +81-52-789-3773

11
12 2) Chief Researcher, Analysis & Simulation Center, Asahi Kasei Corporation
13 2-1 Samejima Fuji-city Shizuoka, 416-8501 Japan
14 sakamoto.ng@om.asahi-kasei.co.jp

15
16 3) Senior Researcher, R&D Laboratories, Asahi Kasei Homes Corporation,
17 2-1 Samejima Fuji-city Shizuoka, 416-8501 Japan
18 matsui.kj@om.asahi-kasei.co.jp

19
20 4) Asst. Prof., Ph.D., Graduate School of Engineering, Tohoku University,
21 Aramaki Aoba 6-6-11-1205, Aoba-ku, Sendai, Miyagi 980-8579, Japan
22 go.igarashi@archi.tohoku.ac.jp

23

24

25 Abstract

26 Meso- and micro-scale structural changes in matured hardened cement paste dried slowly for 1.5 years at different relative
27 humidities (RHs) are evaluated by small-angle X ray scattering profiles covering a q range of 0.017 nm^{-1} – 30 nm^{-1} with a fractal
28 disc-shaped particle analysis and Guinier approximation. The fractal disc-shaped particle analysis revealed that calcium–silicate–
29 hydrate (C–S–H) agglomerations are very thin ($\sim 2.5 \text{ nm}$) and of relatively large width ($\sim 35 \text{ nm}$) under high RH conditions.
30 However, the agglomerations are segmented (in width) into $\sim 10 \text{ nm}$ below an RH of 40%. The Guinier approximation found the
31 possibility that the scattering profiles in the range of 2 nm^{-1} – 8 nm^{-1} correspond to a spacing between C–S–H monolayers and it
32 showed stepwise changes at 40%–50% RH. The stepwise behavior of the distance between C–S–H monolayers may explain a kink
33 in water vapor desorption at around 40% RH.

34

35 **Keywords:** Drying (A); Calcium–silicate–hydrate (C–S–H) (B); Small-Angle X-Ray Scattering (B); Microstructure (B);
36 Adsorption (C);

37

38 1. Introduction

39 Ordinary Portland cement concrete initiates its service life with a relatively high water content condition as the amount of water in
40 the mixture is greater than that required for the cement hydration process. After demolding, the water stored in the concrete
41 evaporates to attain equilibrium with the surrounding atmosphere. Understanding this first drying process is crucial for evaluating the
42 performance of concrete structures as it produces an irreversible alteration of cement hydrates and pore structures during the first
43 drying stage.

44 Calcium-silicate-hydrate (C-S-H, C: CaO, S: SiO₂, H: H₂O, in cement chemistry notation), which is the main hydrate from
45 Portland cement and has a colloidal feature, shows changes in its physical properties during the drying process. These properties
46 include nitrogen gas Brunauer-Emmett-Teller (BET) surface area [1-3], water vapor BET surface area [4, 5] and sorption isotherms
47 [5], and morphology [6]. This characteristic of C-S-H plays a significant role in the property of hardened cement paste (hcp). The
48 microstructure of hcp shows dramatic changes under the first desorption process, altering the strength and Young's modulus of hcp
49 [5, 7-9]. Shrinkage of hcp is also an important phenomenon for the durability of concrete, as hcp shrinkage under a restraint
50 condition produces cracks, which facilitates the penetration of hazardous substances in concrete and reinforcement deterioration. The
51 shrinkage of hcp is predominantly irreversible [5, 10-14]; therefore, analyzing the irreversible alternation of C-S-H under the first
52 desorption process is crucial for understanding and controlling this behavior. This study analyzes this change in C-S-H during the
53 first desorption process through a wide range of small-angle X-ray scattering (SAXS) and water vapor sorption isotherms obtained
54 by a volumetric method with a very short pre-treatment.

55 SAXS or small-angle neutron scattering (SANS) is widely applied for determining the microstructure of materials, especially
56 porous materials and polymers. The merits of SAXS or SANS are as follows: (1) the microstructure over a wide size range (more
57 than three orders of magnitude) can be evaluated simultaneously by considering fractal dimensions or other spatial feature indices,
58 and (2) special pre-treatment of samples is not required. Using a pre-fixed shape model and a size distribution function, quantitative
59 interpretation is possible based on the data obtained.

60 In the field of cement chemistry, surface area changes due to hydration or drying as determined mainly by Porod's law have been
61 previously discussed; some of these reports have concluded that the surface area of hcp changes during drying [15-22]. A building
62 block of C-S-H called a "globule" has been proposed on the basis of the analysis results using SANS [18, 19, 23-28]. The analysis
63 showed that the SANS profiles of cement paste covering a scattering vector $q (=4\pi/\lambda \sin\theta$, where λ denotes the wave length of an X
64 ray or neutron and θ represents the scattering angle) in the range of 0.012 nm⁻¹-1.6 nm⁻¹ and at different degrees of hydration and
65 drying were appropriately reproduced by a fractal model based on a spheroid with an average diameter of ~5 nm. Thomas et al.
66 evaluated the characteristic behavior of C-S-H under the first drying process and the subsequent re-humidifying process by using
67 this spheroid model [29], and different trends of C-S-H gel changes have been suggested according to the relative humidity (RH)
68 range. Recently, Chiang et al. used a fractal model based on disc-shaped globules forming a layered structure for evaluating the
69 SANS profiles of C-S-H, alite paste, and Portland cement paste [30, 31]. From these experiments, the globule, the essential building

70 block of C–S–H, defined through a colloidal model (CM-II) proposed by Jennings [32], is directly evaluated. Interestingly, the size
 71 of the globule determined by Chiang et al. and that by Allen et al. [25] did not agree, possibly because they considered different sizes
 72 of the C–S–H component. A similar analytical method based on a fractal disc-shaped particle model was applied for analyzing the
 73 C–S–H suspension system to evaluate the structure of C–S–H [33] on a scale larger than the size of the globule.

74 In this study, mature white Portland cement paste samples dried under different RHs for more than 1.5 years are evaluated over a
 75 wide scattering vector range obtained by ultra-small-angle X-ray scattering (USAXS), SAXS, and wide-angle X-ray scattering
 76 (WAXS). The results obtained are unified as a single profile and then analyzed by a fractal disc-shaped particle model considering a
 77 fractal dimension distribution in order to quantitatively understand the agglomeration process of colloidal C–S–H under long-term
 78 drying. In addition, water vapor sorption isotherms with a very short-term pretreatment are collected, and the agglomeration
 79 characteristics are discussed.

80

81 2. Experiment

82 2.1 Materials and Specimens

83 White Portland cement with a chemical composition as shown in Table 1 was used to prepare the specimens. A paste (10 L) was
 84 prepared by adding water at a water-to-cement ratio of 0.55, mixed in a 20 L Hobart mixer for 3 min, and remixed for a further 3
 85 min after the paste was scraped from inside the mixer. To minimize segregation, the paste was remixed every 30 min for 6 h. After a
 86 creamy consistency was obtained, the paste was cast into molds and covered with polyvinylidene chloride wrap and wet paper to
 87 avoid loss of water from the specimens. The molds were placed in a thermostatic chamber at a temperature of $20\text{ }^{\circ}\text{C} \pm 1\text{ }^{\circ}\text{C}$. The
 88 specimens were demolded after 4 days and immediately immersed in lime-saturated water, where they were kept for 180 days at
 89 $20\text{ }^{\circ}\text{C}$. After this long curing period, the specimens were considered to be almost fully hydrated; the results of the degree of hydration
 90 has been reported elsewhere [5]. They were then placed in various RH-controlled chambers (11, 20, 30, 40, 50, 60, 70, 80, 90, and
 91 100% RH at $20\text{ }^{\circ}\text{C} \pm 1\text{ }^{\circ}\text{C}$) and allowed to dry slowly for 1.5 years. The demolded hcp specimens were $3\text{ mm} \times 13\text{ mm} \times 300\text{ mm}$
 92 slabs, which could attain equilibrium with the surrounding RH fairly efficiently. The resulting samples that equilibrated slowly at
 93 XX% RH are denoted as “SDSXX”. The details of specimen preparation are provided in the literature [5, 12]. In the case of
 94 SDS100, the specimen placed in limewater was cut for the experiment, and it was constantly wet even when the SAXS profiles
 95 were obtained.

96

97 Table 1. Chemical composition of white cement by X-ray fluorescence elemental analysis*.

Ig. loss (%)	SiO ₂ (%)	Al ₂ O ₃ (%)	Fe ₂ O ₃ (%)	CaO (%)	MgO (%)	SO ₃ (%)	Na ₂ O (%)	K ₂ O (%)	TiO ₂ (%)	P ₂ O ₅ (%)	MnO (%)	Cl (%)
2.93	22.43	4.67	0.16	65.69	0.98	2.51	0.00	0.07	0.17	0.03	0.00	0.00

98 *Conducted by the Taiheiyo Cement Corporation. The data is in mass %.

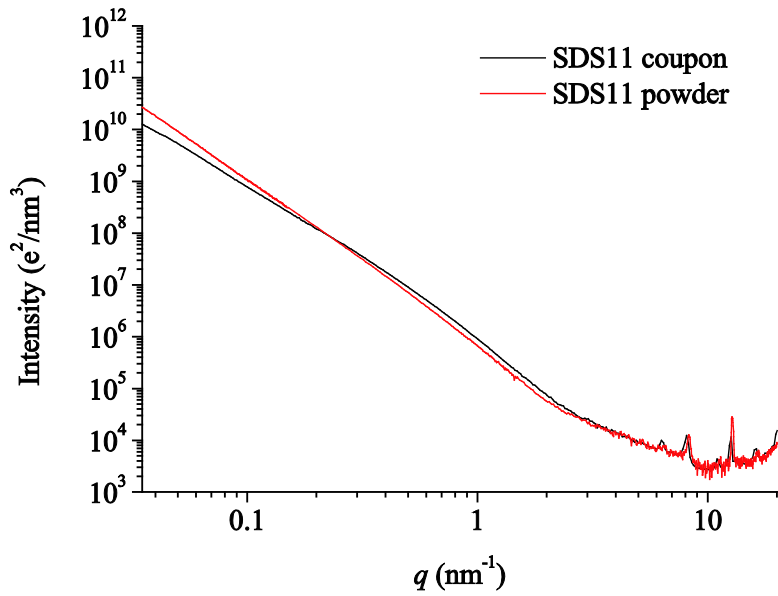
99

100

101 2.2 SAXS and Profile Analysis

102 Coupon samples with dimensions of 0.5 mm × 5 mm × 10 mm were cut from the 3 mm × 13 mm × 300 mm slabs. This
 103 sample shape was based on previous studies [25, 29]. The coupon samples for SDS100, 90, 80, 70, 60, 50, 40, and 11 were
 104 measured without further treatment. A powder sample was not adequate as its dimensions affect the scattering profile. A comparison
 105 between coupon and powder samples is shown in Fig. 1. This figure shows that the sample shape affects the scattering profile,
 106 especially in the low-angle region (i.e., <0.3 nm⁻¹). This suggests that a powder sample can not show the existing structure of hcp.

107



108

109 Fig. 1. Comparison of small angle X-ray scattering profiles for coupon and powder cement paste samples.

110

111 USAXS, SAXS, and WAXS experiments were conducted at the BL08B2 beamline at the Japan synchrotron radiation facility
 112 (SPring-8) using a highly monochromatic beam with a low divergence and a small cross-section. USAXS images were obtained
 113 with a PILATUS 100K detector at a wavelength λ of 0.15 nm, a camera length of 6060 mm, and an exposure time of 10 s. SAXS
 114 images were obtained with a PILATUS 100K detector at a wavelength λ of 0.1 nm, a camera length of 1581 mm, and an exposure
 115 time of 5 s. Finally, WAXS images were obtained with a flat panel detector (FPD) at a wavelength λ of 0.1 nm, a camera length of
 116 62.5 mm, and an exposure time of 5 s. The USAXS/SAXS/WAXS configurations covered a total scattering vector q in the range
 117 0.017 nm⁻¹–30 nm⁻¹; the length of q is given by $q = 4\pi\sin(\theta)/\lambda$, where θ represents the scattering angle.

118 The scattering pattern $I_{obs}(2\theta, \phi)$ measured by a two-dimensional (2-D) detector was azimuthally integrated to obtain the
 119 one-dimensional (1-D) intensity profile $I_{obs}(2\theta)$ as follows:

120

$$121 \quad I_{obs}(2\theta) = \frac{1}{2\pi} \int_0^{2\pi} \frac{I_{obs}(2\theta, \phi) - I_{BG}}{\cos^3 2\theta} d\phi, \quad (1)$$

122

123 where θ : Bragg angle; ϕ : azimuthal angle; and I_{BG} : dark noise.

124 The obtained 1-D intensity profile was converted to absolute units by considering the calibration of the blank cell, exposure time,
125 thickness of samples, transmission factor, and device differences by using Eq. (2). A device factor error of 10% was considered.

126

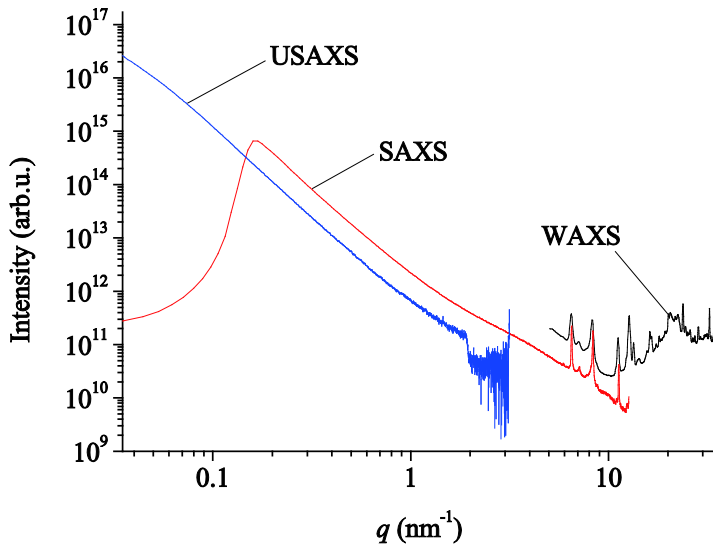
$$127 \quad I(2\theta) = \frac{c}{t} \left[\frac{I_{\text{obs, sample}}(2\theta)}{\text{time}_{\text{sample}} T} - \frac{I_{\text{obs, empty}}(2\theta)}{\text{time}_{\text{empty}}} \right], \quad (2)$$

128

129 where $I_{\text{obs, empty}}(2\theta)$: scattering profile of the blank cell converted to absolute units; $I_{\text{obs, sample}}(2\theta)$: profile obtained by Eq. (1), time :
130 exposure time; t : sample thickness; T : X-ray transmission factor of the sample; and c : device factor.

131 Examples of the profiles of USAXS, SAXS, and WAXS, and the resultant unified profile are shown in Fig. 2.

132



133

134 Fig. 2. Profiles of USAXS, SAXS, and WAXS.

135

136 In this study, the scattering intensity profile was interpreted by comparison of theoretical scattering derived by assuming
137 disc-shaped primary particles arranged in a mass fractal structure.

138 The small-angle scattering absolute intensity can be expressed as follows:

$$139 \quad I(q) = N\rho^2 \langle P(q) \rangle_{t,r} S(q), \quad (3)$$

140 where N : number of particles; ρ : difference in electron densities between solid and pore water or air; $\langle P(q) \rangle$: particle shape factor;

141 $S(q)$: inter-particle structure factor; and q : scattering vector, which is given by $4\pi\sin(\theta)/\lambda$.

142 Assuming the homogeneity of electron density in the disc-shaped particles, the normalized particle shape factor is expressed as

143 follows:

144
$$p(q, r, l) = (2l\pi r^2)^2 \frac{2}{q^2 r^2} \left[1 - \frac{J_1(2qr)}{qr} \right] \left[\frac{\sin(ql)}{ql} \right]^2, \quad (4)$$

145 where r : radius of the disc; l : thickness of the disc; and J_1 : Bessel function.

146 The particle shape factor can then be obtained as shown in Eq. (5) below:

147
$$\langle P(q) \rangle_{l,r} = \int \int P(q, r, l) p_r(r) p_l(l) dr dl, \quad (5)$$

148 where $p_r(r)$ and $p_l(l)$ denote distribution functions for r and l , respectively, and their volume fraction can be expressed by the

149 Shultz–Zimm distribution as shown in Eqs. (6) and (7):

150
$$p_x(x) = \frac{p(x)/V(r,l)}{\int \frac{p(x)}{V(r,l)} dx} \quad (6)$$

151
$$p(x) = \frac{M^M}{\Gamma(M)x_0^M} x^{M-1} \exp\left(-\frac{M}{x_0} x\right) \quad (7)$$

152 Here, $V(r,l)$: volume of disc particles; x : r or l , $\Gamma(x)$: gamma function; $M = (\sigma_x/x_0)^2$; and σ_x : standard deviation of x .

153 Regarding the inter-particle factor $S(q)$, it was assumed that the solid part of hcp consists of disc-like C–S–H aggregations
 154 packed into a fractal-like object, and Eq. (7) was used for the analysis. In Eq. (7), the fractal structure with a fractal dimension D can
 155 be extended to a maximum cutoff dimension of ξ , although 100000 nm was adopted for ξ in the fitting process, which implies that
 156 there is no limit in a practical sense. The inter-particle factor $S(q)$ was obtained by the integration of Eq. (8) as Eq. (9):

157
$$g(r) = \frac{D}{4\pi N} \frac{1}{R_e D} r^{D-3} \exp\left(-\frac{r}{\xi}\right) \quad (8)$$

158
$$S(q) = 1 + \left(\frac{\xi}{R_e}\right)^D \frac{\Gamma(D+1) \sin[(D-1) \tan^{-1}(q\xi)]}{(D-1) [1 + (q\xi)^2]^{(D-1)/2} q\xi}, \quad (9)$$

159 where D : fractal dimension; ξ : cutoff length; and R_e : equivalent spherical radius of the disc-shaped particle, given by $(3/4r^2l)^{1/3}$. Eq.
 160 (8) is the same as the equation used by Chiang et al. [30]. Regarding ξ , the fractal dimension of scattering profiles in the range $q <$
 161 $1/\xi$ should exhibit a small value and this can be observed as an inflection point according to eq. (9). There was, however, no
 162 inflection point observed where the power law changed in the scattering profiles obtained. Based on this fact, the value of ξ was
 163 considered to be greater than 400 nm, and a value of 100000 nm did not conflict with the experimental results, and was considered
 164 reasonable.

165 In addition to the fractal-disc analysis, finer structures were analyzed by the Guinier approximation [34, 35]. The following
 166 equation was used for the analysis:

167
$$I(q) = n \cdot \rho^2 \cdot v^2 \exp\left(-\frac{q^2 R_g^2}{3}\right), \quad (10)$$

168 where v : volume of particles and R_g : radius of gyration.

169

170 (b) Water vapor sorption isotherm measurement

171 Water vapor sorption measurements were conducted by a volumetric method using a water vapor sorption analyzer
 172 (Hydrosorb 1000, Quantachrome). The samples used for this measurement were SDS100, 90, 80, 70, 60, 50, 40, and 11. The hcp

173 samples were first ground in a ball mill to obtain powders with a diameter of 25 μm –75 μm . For pretreatment, the samples were
174 initially dried using a vacuum pump (the theoretical minimum pressure was 6.7×10^{-2} Pa and the observed maximum pressure was
175 30 Pa) and maintained at 105 °C for 30 min using a heating mantle. It should be noted that this pre-drying process might damage the
176 original structure to some degree, but previous research confirmed that the difference of the cement paste structures that were altered
177 under the different RH conditions can be evaluated by this method [5, 12]. A sample of about 20 mg with a pressure tolerance of
178 6.67 Pa and a time tolerance of 120 s was used for each measurement at 20 °C. The measurement points on the adsorption and
179 desorption branches were at $p/p_0 = 0.05$ intervals up to 0.95, and ended at 0.98 (RH = 98%). The water vapor BET areas ($S_{\text{H}_2\text{O}}$) of
180 the adsorption branch were calculated using the BET theory [36], with an area of 0.114 nm² per adsorbed water molecule [37].

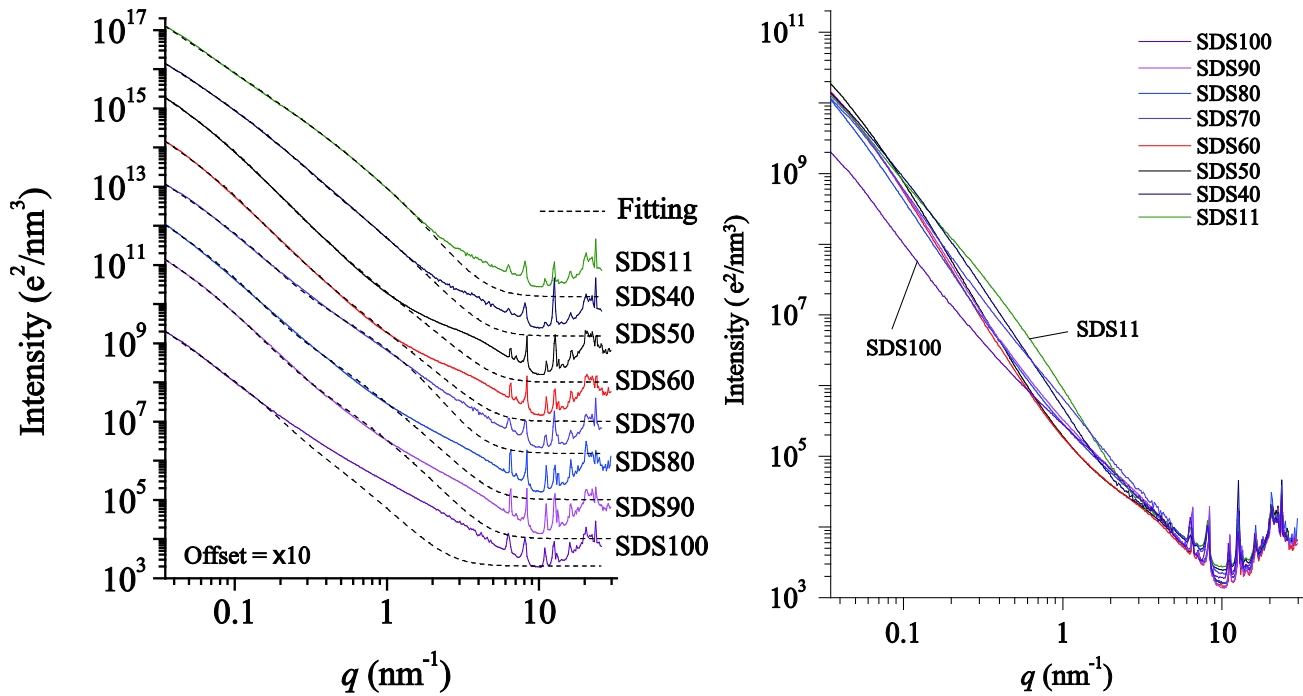
181 3. Experimental Results and Discussion

182 3.1 SAXS

183 Fig. 3 shows the scattering profiles and the fitting results by the fractal disc-shaped particle model. SDS100 shows two
184 shoulders at 0.04 nm^{-1} and 2 nm^{-1} . For SDS90, a shoulder around 0.1 nm^{-1} and a bump around 4 nm^{-1} was observed. This bump
185 around 4 nm^{-1} was observed in all the profiles, and its peak tended to shift to higher angles as the sample was dried.

186 In contrast, a shoulder observed around 0.1 nm^{-1} for SDS90 was still at 0.1 nm^{-1} for SDS80, while it was split into 0.2 nm^{-1}
187 and 1 nm^{-1} for SDS70. This shoulder broadened around 0.2 nm^{-1} and 0.3 nm^{-1} in the case of SDS60 and SDS40, respectively. Finally,
188 a large shoulder was observed around 1 nm^{-1} in the profile for SDS11. The general trend of this shoulder was to move to higher
189 angles, but the behavior was complex at the curing condition of 70%–50% RH.

190



191

192 Fig. 3. Scattering profiles and the fitting profile curves obtained by the proposed fractal disc-shaped particle model (left).

193 Comparison of all the scattering profiles obtained (right).

194

195 The above-mentioned shoulder was the target for the fractal disc-shaped particle analysis. The reason for selecting a disc
196 shape rather than a cylindrical shape is based on a report that described the C–S–H that formed on the outer side of the original
197 cement boundary as being very thin with few layers of calcium silicates [38, 39]. In addition, artificially synthesized C–S–H on a
198 polished calcite surface showed an agglomeration of size $60 \text{ nm} \times 30 \text{ nm} \times 5 \text{ nm}$ [40]. Therefore, the disc shape model was
199 considered to be applicable to the morphology of C-S-H, which was precipitated from the saturated solution.

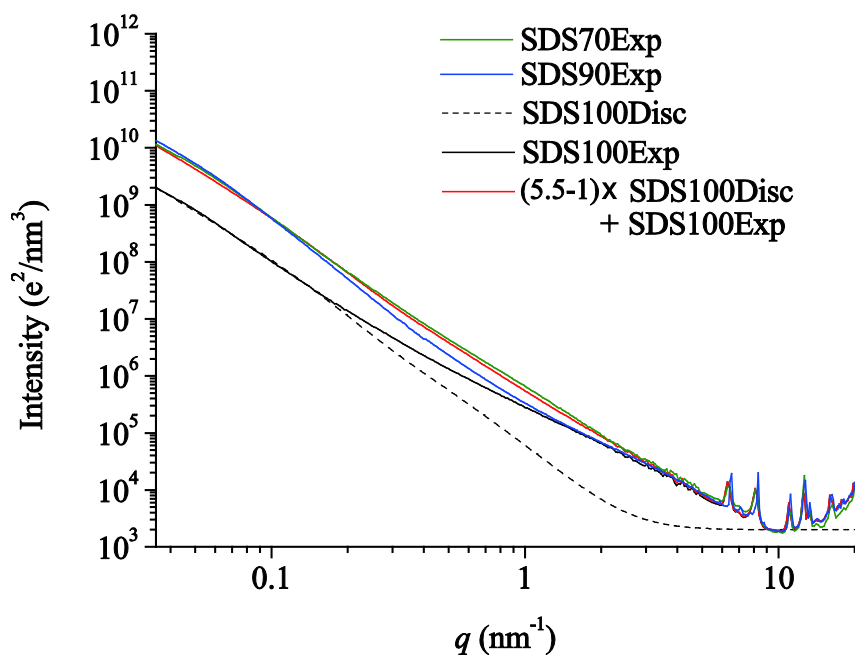
200

201 In a previous research, intensity profiles of hcp for q values below 0.2 nm^{-1} were considered as a surface fractal regime with
the surface of the clinker grains roughening by the formation of hydration products [41]. Furthermore, especially for a q value of

202 approximately 0.002 nm^{-1} , the scattering intensities were produced from Portlandite crystals. On the contrary, the results obtained
203 shown in Fig. 3 indicate the volume fractal behavior was such that $I \propto q^{-x}$, where the scaling exponent x was about 2.53 (2.47–2.58)
204 for a q value of approximately 0.02 nm^{-1} . In addition, the measured q range in the present study was $0.017\text{--}15 \text{ nm}^{-1}$; therefore, the
205 scattering intensities from Portlandite crystals could be ignored. At the same time, the impact on unhydrated cement on the scattering
206 intensity could also be neglected as the degree of hydration was greater than 95% [5]. Based on these facts, only the volume fractal
207 packing of disc-shaped C–S–H agglomeration was considered for the intensity analysis. Note that the previous reports have pointed
208 out that the scattering profiles affected by the drying process reflect the morphological change of outer (or low-density) C–S–H [29,
209 42, 43].

210 Before analyzing the fitting results, the density of the discs was addressed. In case of SDS100, the result of fractal disc
211 analysis is shown in Figs. 3 and 4 and in Table 2. In this case, solid discs were submerged in pore water. Therefore, their electron
212 density contrast differed from that of the other samples. Hence, based on this result, the profiles of fractal disc structures in air were
213 estimated considering the ratio of electron density contrasts of solid–gas to solid–liquid. The electron densities of water, air, and C–
214 S–H were 334 nm^{-3} , 0 nm^{-3} , and 581 nm^{-3} , respectively, where the composition of C–S–H was assumed to be $\text{C}_{1.7}\text{SH}_{4.0}$ and its
215 density was 1.87 g/cm^3 [44]. The square of the contrast ratio of solid–gas to solid–liquid resulted in $5.5 (= 581^2/(581 - 334)^2)$. Based
216 on this and considering that the SAXS profiles of SDS100 contained the fractal disc profiles of solid-liquid contrast, the profiles of
217 SDS100 in the air was obtained by $(5.5 - 1) \times \text{SDS100Disc} + \text{SDS100Exp}$, where the notations “Disc” and “Exp” indicate the
218 profiles obtained from the fractal disc analysis and the experiment, respectively, as shown in Fig. 4. This estimated profile was very
219 similar to that of SDS70, but it differed from that of SDS90 in the range of $0.2 \text{ nm}^{-1}\text{--}1 \text{ nm}^{-1}$. The range in which this difference was
220 observed is not the range corresponding to a Kelvin radius ($\sim 5 \text{ nm}$, and $\sim 1.25 \text{ nm}^{-1}$ in q) at 90% RH in 293 K at which the liquid–
221 gas interface was formed. Based on these data, it could be concluded that the fractal disc-shaped particle corresponds to the wet C–
222 S–H solid structure and the profiles of samples dried slowly under 90% RH or less reflected the structure of wet C–S–H. In addition,
223 the fine structure observed around 3 nm^{-1} could not be fitted by the fractal disc-shaped particle analysis and did not have an open
224 solid–gas interface.

225



226

227 Fig. 4. Scattering profiles of SDS100, SDS90, and SDS70 (SDS100Exp, SDS90Exp, and SDS70, respectively). The results of
 228 fractal disc-shaped particle analysis are shown as SDS100Disc. Based on the liquid-gas and air-gas electron density contrast, the
 229 profile of SDS100 in air was estimated as $4.5 \times \text{SDS100Disc} + \text{SDS100Exp}$.

230

231

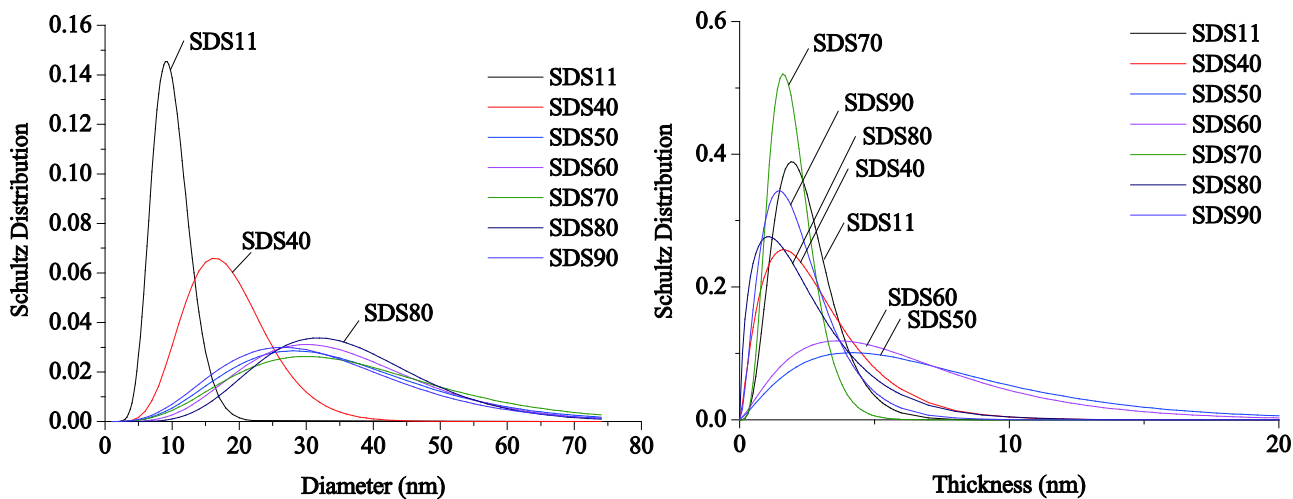
Table 2. Results of fitting of SAXS profiles by fractal disc-shaped particle analysis.

	SDS11	SDS40	SDS50	SDS60	SDS70	SDS80	SDS90	SDS100
Fractal dimension	2.58	2.47	2.47	2.47	2.47	2.47	2.47	2.58
Representative radius (nm)	2.8	3.8	6.4	6.3	5.5	5.5	4.6	5.0
Average disc diameter (nm)	9.9	18.5	34.9	37.4	29.4	36.1	32.9	24.6
SD of disc diameter (nm)	2.8	6.4	15.3	16.6	8.6	12.5	14.5	6.9
Average thickness of disc (nm)	2.5	2.9	7.5	6.4	2.0	2.6	2.3	3.3
SD of thickness of disc (nm)	1.1	2.0	4.9	4.2	0.8	2.0	1.4	2.4

232

* Coefficients of variation of fractal dimension and representative radius are 0.97% and 2.59% respectively.

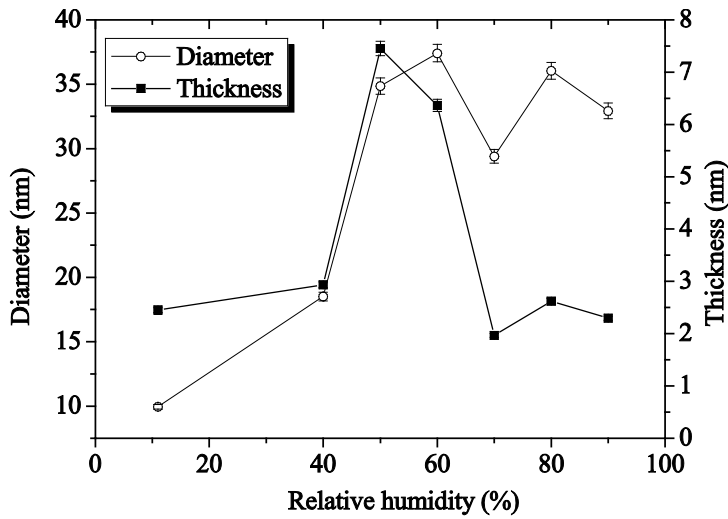
233



234

235
236

Fig. 5. Distribution of the diameter (left) and thickness (right) of discs as obtained by fitting the scattering profiles.



237

Fig. 6. General trend of diameter and thickness of the discs as a function of relative humidity. The error bars represent 1σ .

238
239

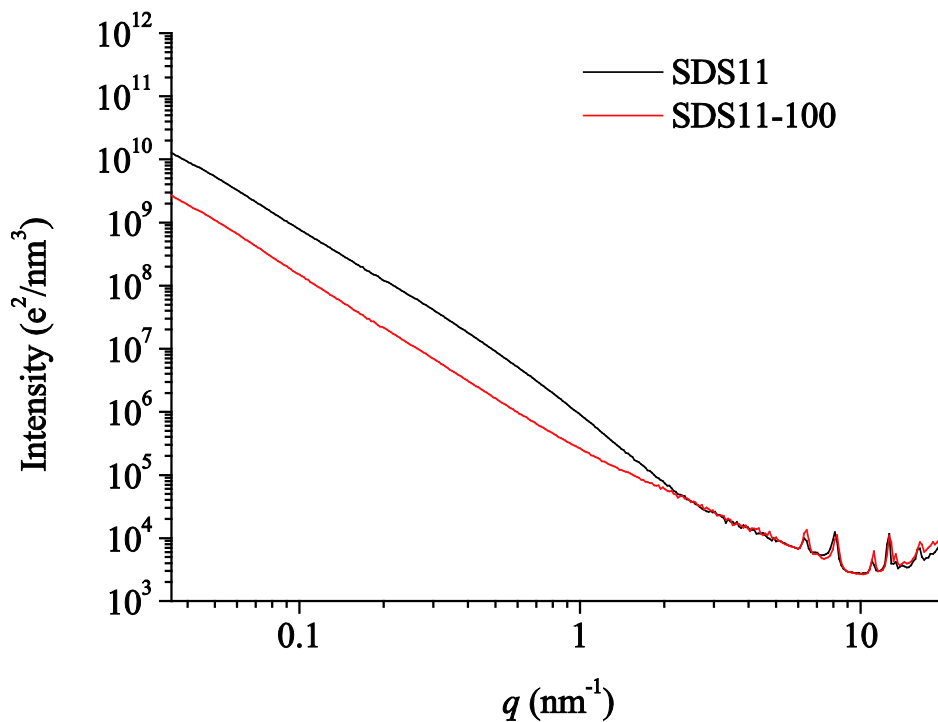
240 The results obtained from the profiles of the fractal disc-shaped particle analysis are summarized in Table 2. The Schultz–
241 Zimm distributions of diameter and thickness of the discs obtained by fitting the scattering profiles are shown in Fig. 5. The average
242 diameter and thickness of the discs as a function of relative humidity for the samples subjected to long-term drying are summarized
243 in Fig. 6. The disc diameter decreased as the dehydration of the samples progressed. In the range above 50% RH, the diameter
244 ranged between 25 nm–37 nm. As seen in Fig. 4, the distributions of the diameters showed similarity. Therefore, this diameter range
245 was considered to be the agglomeration unit for outer C–S–H in matured cement paste, which resulted from the precipitation process.
246 This size was almost consistent with the results obtained by atomic force microscopy (AFM) [40]. However, the size decreased to 17
247 nm in SDS40 and 10 nm in SDS11, and the distribution of the diameter became narrower with further dehydration. These two
248 diameter values were consistent with the diameter of spherical C–S–H particles proposed by Powers and Brownyard based on
249 sorption measurements [45].

250 The thickness of the discs showed an almost constant value of 2 nm–2.5 nm, except in the case of SDS60 and SDS50. If the
251 atomic scale structure of C–S–H was similar to that of tobermorite or jennite [38, 46, 47], this size indicated about two units of them,
252 which was very consistent with a previous observation [38]. On the contrary, the thickness of the discs in the cases of SDS60 and
253 SDS50 showed a different trend and were 6.5 nm–7.5 nm, which corresponded to 3–4 times the thickness of the other samples.
254 Correspondingly, the distribution of disc thicknesses for SDS50 and SDS60 showed different trends than those for the other samples.
255 As there was consistency among SDS100, SDS90, SDS80, SDS70, SDS40, and SDS11 and as it seemed impossible that the
256 structure grew in the 002 direction in the specific relative humidity condition, C–S–H agglomerations were deduced to be compiled
257 during these RH conditions due to cohesion produced by an increase in surface energy. At the same time, due to this compiled

258 structure, the apparent structure seemed thicker in the cases of SDS60 and SDS50. This meso-scale trend was also suggested by
259 short-term water vapor sorption isotherms [5]. This will be discussed later.

260 Based on the trends of disc diameter and thickness, the agglomeration of C–S–H may have decomposed into small particles
261 as the samples dried, especially in the range below 40% RH. These small particles could be considered to be the basic unit of the C–
262 S–H structure based on the CM-II model proposed by Jennings [32], but the size was not comparable to that proposed by other
263 studies [25, 32, 41].

264 Smaller scale, wider angle regions were also analyzed in this study. In Fig. 3, we observed that there was another structure
265 from 2 nm^{-1} – 8 nm^{-1} , where the difference between the obtained profiles and the fitted profiles from the disc-shaped particle model
266 was visible. No report is available in the open literature about the structure in this region due to the scarcity of data in this range.
267 Chiang, et al. [30] analyzed the basal spacing in the C–S–H globule, but the scattering profiles in this study did not have any sharp
268 peaks in this region. Even in the case of tobermorite synthesis under autoclave conditions, the sharp peak around 2 nm^{-1} – 8 nm^{-1} was
269 not reproduced in our measurement system [48]. This fine structure did not show a dramatic change from SDS90 to SDS11, and
270 based on Fig. 4, we did not consider that this structure was affected by a liquid–gas interface. In addition to Fig. 4, an additional
271 measurement was conducted, that is water submerged SDS11 (called SDS11-100). The sample of SDS11 was cut into a thin coupon
272 and submerged in a saturated portlandite solution for 5 days, and then the SAXS profiled was obtained. The result of SDS11-100
273 was compared with SDS11 in Fig. 7. As shown in Fig. 7, the structure reflected in the SAXS profile around 2 nm^{-1} – 8 nm^{-1} was not
274 affected by water immersion, while the water could penetrate into almost all the available pores in cement paste.



275
276 Fig. 7. Comparison of the scattering profiles of SDS11 and SDS11-100.

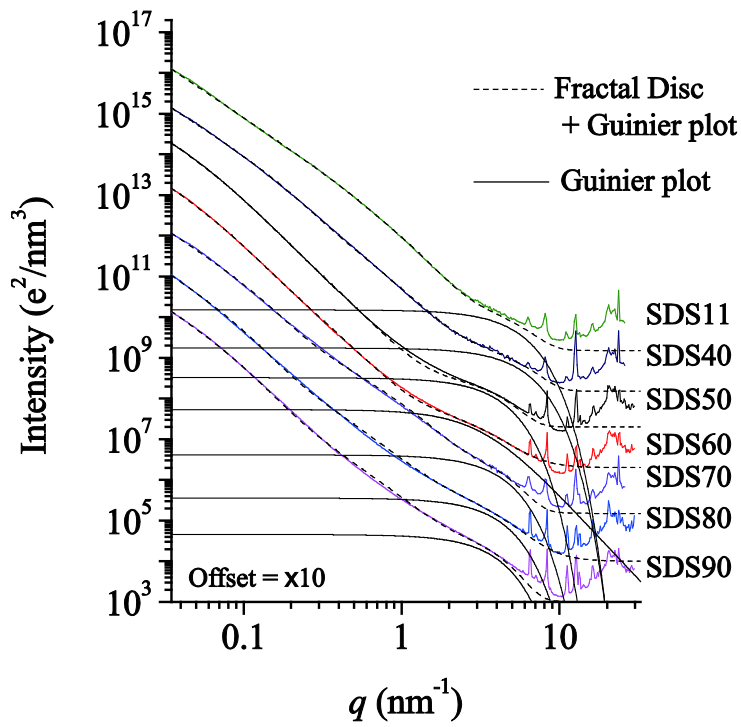
277

278

279 Based on the Guinier approximation, the representative size (R_g) was evaluated for this fine structure. Results of the fitting
280 are shown in Fig. 8 and the obtained R_g values and volumetric ratios (R_v) of this isolated fine structure (with the reference volume
281 being that of the fine structures in SDS11) are shown in Fig. 9. Note that we assumed that the number of fine particles would not
282 change by slow drying, and based on this assumption, R_v was obtained.

283 In Fig. 9, the R_g value obtained shows a stepwise trend as a function of relative humidity for long-term drying. There was a
284 sudden drop between SDS40 and SDS50. Interestingly, R_v also showed the same trend. This is quite unnatural since the cubic law
285 must be satisfied if R_g changes in a volumetric manner. Therefore, assuming that the number of these isolated fine particles
286 remained constant, the particles deformed one dimensionally. If the target shape as composed by pores, it was very strange that the
287 pores were deformed in one direction under the drying condition, where the bulk matrix showed homogenous shrinkage. It is
288 suggested that the attribution of the target structure to the isolated pores in the cement paste matrix was denied due to this
289 characteristic behavior.

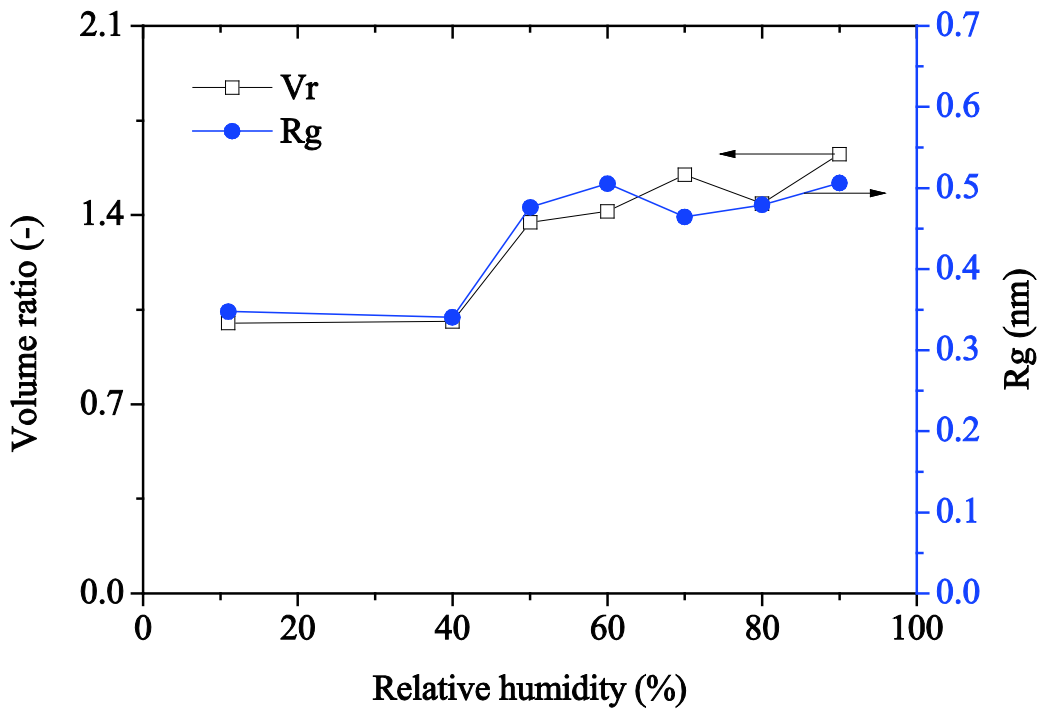
290 This characteristic behavior corresponded to the behaviors of C–S–H. The basal spacing change in synthesized C–S–H(I)
291 with Ca/Si atomic ratios of 1.25 and 1.5 also showed a stepwise deformation, and the jump could be found between 50% RH and
292 40% RH [49]. The C–S–H(I) used in this experiment had a 002 peak, which indicates that C–S–H(I) crystals grew in the (002)
293 direction and had a structural limitation. However, the present C–S–H existing in matured cement paste was not structurally grown
294 and the peak in the 002 plane could not be observed. Therefore, in the direction perpendicular to this plane, C–S–H might have had
295 some freedom to grow. Consequently, in this study, the hypothesis that the scattering profile around 4 nm^{-1} represented the structure
296 of C–S–H, such as the spacing between C–S–H monolayers is proposed. This hypothesis may be supported by the concepts and
297 experimental results of Chiang, et al. [30]; however, the scattering profiles were not reproduced in this study.



298

299

Fig. 8. Comparison of scattering profiles with fitted profiles obtained by the disc-shaped and spherical models.



300

Fig. 9. Representative size (Rg) by the Guinier approximation and volumetric ratio (Vr) of the fine structure as a function of relative humidity for long-term drying.

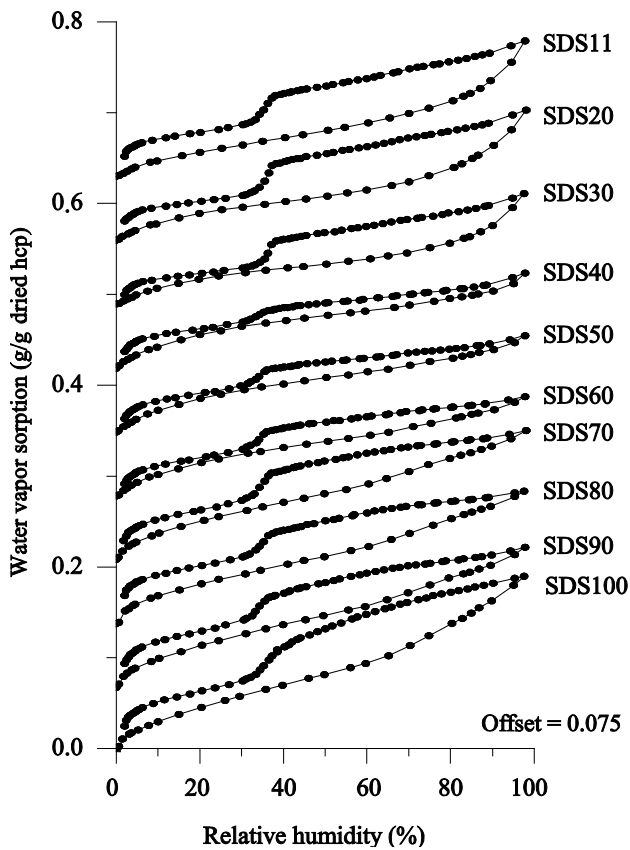
303

3.2 Water vapor sorption isotherm

Results of water vapor sorption isotherms of cement paste dried under different relative humidities are summarized in Fig. 10. In

306 general, the amount of total sorption (the sorption amount at 98% RH) decreased from SDS100 to SDS40 and then increased from
 307 SDS40 to SDS11. A sudden drop (called a kink) around 40% RH in the desorption process was clearly shown in all the cases.
 308 Especially, in the cases of SDS60, SDS50, and SDS40, there was a meeting point of the adsorption and desorption processes at
 309 30%–40% RH and a double loop was observed. This was quite consistent with the case of length-change isotherms of SDS40 and
 310 SDS50 [12]. However, the trends of SDS30, SDS20, and SDS11 were not consistent.

311



312

313 Fig. 10. Sorption isotherms of the cement paste samples dried under different relative humidities.

314

315 To evaluate the change in sorption behavior of the samples, typical sorption isotherms of SDS100, SDS70, SDS40, and
 316 SDS11 are compared in Fig. 11 (left). The statistical thicknesses [50] in the adsorption and desorption processes are plotted in Fig. 11
 317 (right).

318 The top left of Fig. 11 indicates that drying from 100% RH to 40% RH decreased the total sorption and the first layer
 319 adsorption, and SDS40 showed the smallest sorption among all the samples. In addition, when the samples were further dried, the
 320 total sorption increased unlike the trend shown for the higher RH conditions, and the total sorption of SDS11 was greater than that of
 321 SDS70. In addition, in the case of SDS11, a hysteresis in the low-RH range (below 30% RH) was clearly visible.

322 The sorption thicknesses in the adsorption and desorption processes of the samples are compared in Fig. 11 (right).

323 Adsorption and desorption processes of SDS100, SDS70, SDS40, and SDS11 showed a similar trend below 30% RH. In the

324 adsorption process, when SDS100, SDS70, and SDS40 were compared, the statistical thickness curves showed branches at lower
325 RHs, and the samples dried at lower RH showed smaller sorption. The sorption sites or pores corresponding to the water sorption
326 from 40% to 98% RH decreased by drying in an RH range of 100% to 40%.

327 The water vapor sorption should commence from the sorption in the C–S–H layers since the internal spaces between the C–
328 S–H monolayers (CaO plane + Silicate dimers) have a strong adsorption potential due to overlapping of the adsorption potential
329 from each C–S–H monolayer and therefore water molecules must be adsorbed strongly between the C–S–H monolayers. A
330 previous report [12] proposed that there is a movable C–S–H monolayer and the distance between the C–S–H monolayers is
331 dynamically changed by drying and re-humidifying. Because there is no structural limitation in maintaining the distance between the
332 C–S–H monolayers, such as Si-Q3 sites, and randomly attached silicate dimers on the CaO layer will create a twisted structure,
333 crystal growth in the 002 direction is difficult [51]. These structural characteristics must change the distance between C–S–H
334 monolayers during the sorption process.

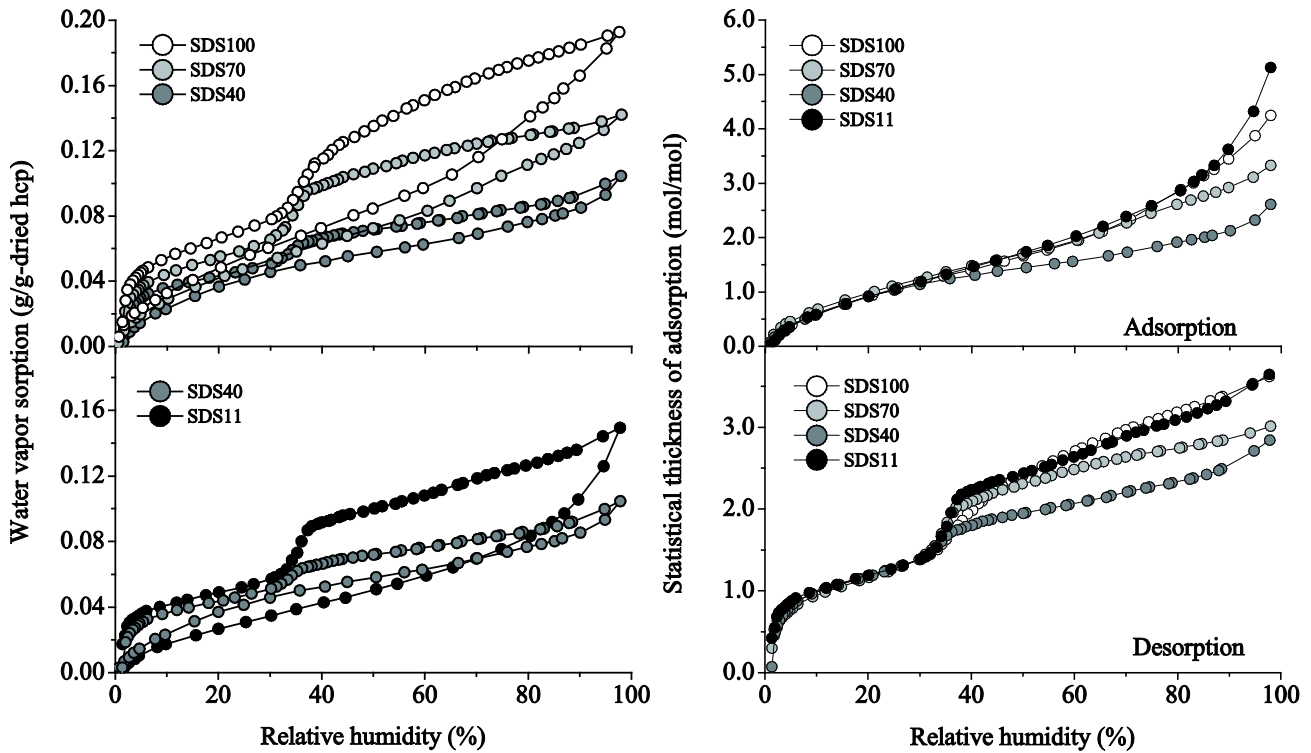
335 Based on the SAXS profile analysis, in the drying process from 100% to 40% RH, couples of C–S–H monolayers were
336 stacked and attached to each other, and the average compilation attained 5–7 C–S–H layers, thus constraining the freedom to absorb
337 the water molecules between the layers. Therefore, the total sorption amount was reduced from 100% to 40% RH.

338 Below 40% RH, the total sorption was regained and the statistical thickness of sorption was almost the same as that of
339 SDS100. This indicates that the movable C–S–H monolayers or open spaces around C–S–H agglomerations provided the freedom
340 to absorb water molecules. This production of space that enables absorption is explained by the segmentation of C–S–H
341 agglomeration due to the drying process as suggested by disc analysis results. Small segmented particles must be movable and may
342 facilitate the freedom to absorb water molecules.

343 The possible driving force of this segmentation is the 1-D shrinking behavior of the fine structures. Dehydration between
344 winding C–S–H monolayers shortens the distance between C–S–H monolayers, and randomly wound layers can be broken by this
345 closing process. During this process, some spaces between the C–S–H monolayers are broken and the layers peel off, changing into
346 an outer surface where the water sorption potential is low. Resultantly, this segmentation process causes a reduction in the BET area
347 (S_{H_2O}) in the adsorption process, as shown in Fig. 12. (The term “BET surface area” is not used in this paper as we assume that water
348 is absorbed in the spaces between the C–S–H monolayers which is not the BET surface area. Therefore, following the ISO
349 recommendation [52], the term “BET area” is used in this study). There is a clear decreasing trend of S_{H_2O} for the adsorption process
350 from SDS11 to SDS40.

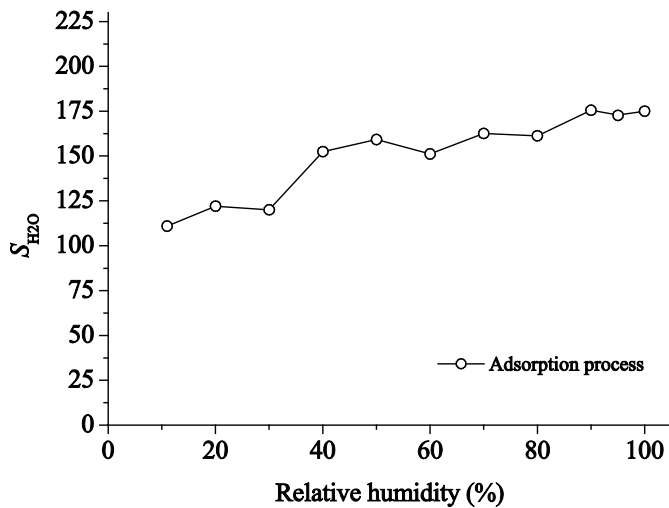
351 In addition, it should be noted that coincidentally, the RH at the point a kink was observed in the water vapor desorption profile
352 was almost the same RH when a stepwise change in fine structures was obtained in the SAXS profiles. This coincidence also
353 suggests that the fine structure represented the distance between the C–S–H monolayers and a sudden change around 40% RH.
354 Moreover, the kink in the desorption process could be attributed to the sudden change in the distance between C–S–H monolayers.
355 This water molecule behavior under the sorption and desorption process with the dynamic structural change of C–S–H monolayers

356 was in contrast to previous models in which water molecules were adsorbed in the stable C–S–H interlayers firstly and then
 357 absorbed in gel pores according to the corresponding RH region [53-55]. These previous sorption models for hardened cement
 358 in line with a model proposed by Barrett, et al. [56], [57], in which a combination of capillary condensation and physical adsorption
 359 composed the sorption isotherm of porous materials. The new model, however, agreed well with previous layered structures of clay
 360 minerals [58-63], and our new C–S–H model in which divalent (Ca^{2+}) and univalent (CaOH^+) solvated cations were incorporated to
 361 balance the negative charge of the basal sheet [64].



362
 363 Fig. 11. Typical sorption isotherm changes for paste samples dried under different relative humidities. Top left: Comparison of
 364 SDS100, SDS70, and SDS40. Bottom left: Comparison of SDS40 and SDS11. Top right: Difference in the statistical thickness of
 365 adsorption of SDS100, SDS70, SDS40, and SDS11. Bottom right: Difference in the statistical thickness of desorption of SDS100,
 366 SDS70, SDS40, and SDS11.

367



368

369

Fig. 12. The BET area of cement paste samples dried under different relative humidities.

370

371

4. Conclusion

372

373

374

375

376

377

378

379

380

381

382

383

384

385

386

387

388

389

390

Acknowledgements

391

392

The experiments in this study were partly sponsored by the Nuclear Regulation Authority (NRA) of Japan and JSPS KAKENHI Grant Number 15H04077. The measurements of the water vapor sorption isotherms were conducted by Mr. Daichi Hashimoto

393 (Master course student, Nagoya University) to whom the authors would like to express their gratitude.
394

- 396 [1] C.M.Hunt, L.A.Tomes, R.L.Blaine, Some Effects of Aging on the Surface Area of Portland Cement Paste, Journal of Research of the
397 National Bureau of Standards, 64A (1960) 163-169.
- 398 [2] L.J. Parrott, W. Hansen, R.L. Berger, Effect of first drying upon the pore structure of hydrated alite paste, Cement and Concrete Research,
399 10 (1980) 647-655.
- 400 [3] G.G. Litvan, R.E. Myers, Surface area of cement paste conditioned at various relative humidities, Cement and Concrete Research, 13
401 (1983) 49-60.
- 402 [4] L.A. Tomes, C.M. Hunt, R.L. Blaine, Some Factors Affecting the Surface Area of Hydrated Portland Cement as Determined by
403 Water-Vapor and Nitrogen Adsorption, Journal of Research of the National Bureau of Standards, 59 (1957) 357-364.
- 404 [5] I. Maruyama, Y. Nishioka, G. Igarashi, K. Matsui, Microstructural and bulk property changes in hardened cement paste during the first
405 drying process, Cement and Concrete Research, 58 (2014) 20-34.
- 406 [6] P.C. Fonseca, H.M. Jennings, The effect of drying on early-age morphology of C-S-H as observed in environmental SEM, Cement and
407 Concrete Research, 40 (2010) 1673-1680.
- 408 [7] M.N. Haque, D.J. Cook, The effect of water sorption on the dynamic modulus of elasticity of desiccated concrete materials, Mat Constr,
409 9 (1976) 407-410.
- 410 [8] B. Zech, M. Setzer, The dynamic elastic modulus of hardened cement paste. Part I: A new statistical model—water and ice filled pores,
411 Mater Struct, 21 (1988) 323-328.
- 412 [9] S.E. Pihlajavaara, A review of some of the main results of a research on the ageing phenomena of concrete: Effect of moisture conditions
413 on strength, shrinkage and creep of mature concrete, Cement and Concrete Research, 4 (1974) 761-771.
- 414 [10] R.A. Helmuth, D.H. Turk, The Reversible and Irreversible Drying Shrinkage of Hardened Portland Cement and Tricalcium Silicate
415 Pastes, Journal of the PCA Research and Development Laboratories, 9 (1967) 8 - 21.
- 416 [11] I. Maruyama, Origin of Drying Shrinkage of Hardened Cement Paste: Hydration Pressure, Journal of Advanced Concrete Technology,
417 8 (2010) 187-200.
- 418 [12] I. Maruyama, G. Igarashi, Y. Nishioka, Bimodal behavior of C-S-H interpreted from short-term length change and water vapor sorption
419 isotherms of hardened cement paste, Cement and Concrete Research, 73 (2015) 158-168.
- 420 [13] W. Hansen, Drying Shrinkage Mechanisms in Portland Cement Paste, Journal of the American Ceramic Society, 70 (1987) 323-328.
- 421 [14] A. Bentur, R.L. Berger, F.V. Lawrence Jr, N.B. Milestone, S. Mindess, J.F. Young, Creep and drying shrinkage of calcium silicate pastes
422 III. A hypothesis of irreversible strains, Cement and Concrete Research, 9 (1979) 83-95.
- 423 [15] D.N. Winslow, S. Diamond, Specific Surface of Hardened Portland Cement Paste as Determined by Small-Angle X-Ray Scattering,
424 Journal of the American Ceramic Society, 57 (1974) 193-197.
- 425 [16] J. Kropp, T. Gräfeneker, H.K. Hilsdorf, Characterization of the microstructure of hydrated cement paste by small angle X-ray
426 scattering, in: J.W. Arrowsmith (Ed.) Principles and Applications of Pore Structural Characterization, Bristol, 1985, pp. 83-96.
- 427 [17] J.J. Völkl, R.E. Beddoe, M.J. Setzer, The specific surface of hardened cement paste by small-angle X-ray scattering effect of moisture
428 content and chlorides, Cement and Concrete Research, 17 (1987) 81-88.
- 429 [18] J.J. Thomas, H.M. Jennings, A.J. Allen, The surface area of cement paste as measured by neutron scattering: evidence for two C-S-H
430 morphologies, Cement and Concrete Research, 28 (1998) 897-905.
- 431 [19] J.T. Jeffrey, M.J. Hamlin, J.A. Andrew, The Surface Area of Hardened Cement Paste as Measured by Various Techniques, Concrete
432 Science and Engineering, (1999) 45-64.
- 433 [20] R.E. Beddoe, K. Lang, Effect of moisture on fractal dimension and specific surface of hardened cement paste by small-angle X-ray
434 scattering, Cement and Concrete Research, 24 (1994) 605-612.
- 435 [21] M. Kriechbaum, G. Degovics, P. Laggner, J. Trithart, Investigations on cement pastes by small-angle X-ray scattering and BET: the
436 relevance of fractal geometry, Advances in Cement Research, 6 (1994) 93-101.
- 437 [22] F. Häußler, M. Hempel, H. Baumbach, J. Trithart, Nanostructural investigations of hydrating cement pastes produced from cement
438 with different fineness levels, Advances in Cement Research, 13 (2001) 65-73.
- 439 [23] D. Pearson, A. Allen, C.G. Windsor, N. Alford, D.D. Double, An investigation on the nature of porosity in hardened cement pastes
440 using small angle neutron scattering, Journal of Materials Science, 18 (1983) 430-438.
- 441 [24] A.J. Allen, R.C. Oberthur, D. Pearson, P. Schofield, C.R. Wilding, Development of the fine porosity and gel structure of hydrating

442 cement systems, *Philosophical Magazine Part B*, 56 (1987) 263-288.

443 [25] A. Allen, Time-resolved phenomena in cements, clays and porous rocks, *Journal of Applied Crystallography*, 24 (1991) 624-634.

444 [26] A.J. Allen, R.A. Livingston, Relationship between differences in silica fume additives and fine-scale microstructural evolution in
445 cement based materials, *Advanced Cement Based Materials*, 8 (1998) 118-131.

446 [27] J.J. Thomas, J.J. Chen, A.J. Allen, H.M. Jennings, Effects of decalcification on the microstructure and surface area of cement and
447 tricalcium silicate pastes, *Cement and Concrete Research*, 34 (2004) 2297-2307.

448 [28] A.J. Allen, J.J. Thomas, H.M. Jennings, Composition and density of nanoscale calcium-silicate-hydrate in cement, *Nat Mater*, 6 (2007)
449 311-316.

450 [29] J.J. Thomas, A.J. Allen, H.M. Jennings, Structural Changes to the Calcium-Silicate-Hydrate Gel Phase of Hydrated Cement with Age,
451 Drying, and Resaturation, *Journal of the American Ceramic Society*, 91 (2008) 3362-3369.

452 [30] W.-S. Chiang, E. Fratini, P. Baglioni, D. Liu, S.-H. Chen, Microstructure Determination of Calcium-Silicate-Hydrate Globules by
453 Small-Angle Neutron Scattering, *The Journal of Physical Chemistry C*, 116 (2012) 5055-5061.

454 [31] W.-S. Chiang, E. Fratini, F. Ridi, S.-H. Lim, Y.-Q. Yeh, P. Baglioni, S.-M. Choi, U.S. Jeng, S.-H. Chen, Microstructural changes of
455 globules in calcium-silicate-hydrate gels with and without additives determined by small-angle neutron and X-ray scattering, *Journal of*
456 *Colloid and Interface Science*, 398 (2013) 67-73.

457 [32] H.M. Jennings, Refinements to colloid model of C-S-H in cement: CM-II, *Cement and Concrete Research*, 38 (2008) 275-289.

458 [33] L. Nicoleau, T. Gadt, L. Chitu, G. Maier, O. Paris, Oriented aggregation of calcium silicate hydrate platelets by the use of comb-like
459 copolymers, *Soft Matter*, 9 (2013) 4864-4874.

460 [34] A. Guinier, G. Fournet, *Small angle scattering of X-rays*, J Wiley & Sons, New York, (1955).

461 [35] O. Gratter, O. Kratky, Particle scattering. Special cases, in: *Small angle X-ray scattering*, Academic press, London, 1982.

462 [36] S. Brunauer, P.H. Emmett, E. Teller, Adsorption of Gases in Multimolecular Layers, *Journal of the American Chemical Society*, 60
463 (1938) 309-319.

464 [37] R.S. Mikhail, S.A. Selim, Adsorption of organic vapors in relation to the pore structure of hardened Portland cement pastes, in:
465 *Proceedings of Symposium on Structure of Portland Cement Paste and Concrete*, Highway Research Board Special Report 90,
466 Washington D. C., 1966, pp. 123-134.

467 [38] I.G. Richardson, Tobermorite/jennite- and tobermorite/calcium hydroxide-based models for the structure of C-S-H: applicability to
468 hardened pastes of tricalcium silicate, β -dicalcium silicate, Portland cement, and blends of Portland cement with blast-furnace slag,
469 metakaolin, or silica fume, *Cement and Concrete Research*, 34 (2004) 1733-1777.

470 [39] A. Baronnet, O. Grauby, Structure, texture, composition and growth mechanism of calcium silicate hydrate (C-S-H) seen by TEM at
471 the nanoscale, in: *Microstructure, setting and aging of cement From soft matter physics to sustainable materials*, Monte Verita, 2012.

472 [40] A. Nonat, The structure and stoichiometry of C-S-H, *Cement and Concrete Research*, 34 (2004) 1521-1528.

473 [41] A.J. Allen, J.J. Thomas, Analysis of C-S-H gel and cement paste by small-angle neutron scattering, *Cement and Concrete Research*,
474 37 (2007) 319-324.

475 [42] H.M. Jennings, Colloid model of C-S-H and implications to the problem of creep and shrinkage, *Mater Struct*, 37 (2004) 59-70.

476 [43] H.M. Jennings, J.J. Thomas, J.S. Gevrenov, G. Constantinides, F.-J. Ulm, A multi-technique investigation of the nanoporosity of
477 cement paste, *Cement and Concrete Research*, 37 (2007) 329-336.

478 [44] J.F. Young, W. Hansen, Volume Relationships for C-S-H Formation Based on Hydration Stoichiometries, *MRS Proceedings*, 85 (1986)
479 313-322.

480 [45] T.C. Powers, T.L. Brownyard, Studies of the Physical Properties of Hardened Portland Cement Paste
481 Part 3. Theoretical Interpretation of Adsorption Data, *Journal of the American Concrete Institute*, 18 (1946) 469-504.

482 [46] I.G. Richardson, The calcium silicate hydrates, *Cement and Concrete Research*, 38 (2008) 137-158.

483 [47] I. Richardson, Model structures for C-(A)-S-H(I), *Acta Crystallographica Section B*, 70 (2014) 903-923.

484 [48] K. Matsui, N. Sakamoto, J. Watanabe, S. Matsuno, ANALYSIS OF CALCIUM-SILICATE-HYDRATES ON THE
485 TOBERMORITE FORMATION PROCESS BY ULTRA SMALL-ANGLE X-RAY SCATTERING, *Cement Science and Concrete*
486 *Technology*, 68 (2014) 53-60.

487 [49] P. Bayliss, Further interlayer desorption studies of CSH(I), *Cement and Concrete Research*, 3 (1973) 185-188.

488 [50] R. Badmann, N. Stockhausen, M.J. Setzer, The statistical thickness and the chemical potential of adsorbed water films, *Journal of*
489 *Colloid and Interface Science*, 82 (1981) 534-542.

- 490 [51] E.M. Gartner, A proposed mechanism for the growth of C-S-H during the hydration of tricalcium silicate, *Cement and Concrete*
491 *Research*, 27 (1997) 665-672.
- 492 [52] ISO 9277:2010(en) ANNEX C., Determination of the specific surface area of solids by gas adsorption — BET method, in, 2010, pp.
493 <https://www.iso.org/obp/ui/#iso:std:iso:9277:ed-9272:v9271:en:sec:C>.
- 494 [53] M.B. Pinson, E. Masoero, P.A. Bonnaud, H. Manzano, Q. Ji, S. Yip, J.J. Thomas, M.Z. Bazant, K.J. Van Vliet, H.M. Jennings,
495 Hysteresis from Multiscale Porosity: Modeling Water Sorption and Shrinkage in Cement Paste, *Physical Review Applied*, 3 (2015) 064009.
- 496 [54] H.M. Jennings, A. Kumar, G. Sant, Quantitative discrimination of the nano-pore-structure of cement paste during drying: New insights
497 from water sorption isotherms, *Cement and Concrete Research*, 76 (2015) 27-36.
- 498 [55] V. Baroghel-Bouny, Water vapour sorption experiments on hardened cementitious materials: Part I: Essential tool for analysis of hygral
499 behaviour and its relation to pore structure, *Cement and Concrete Research*, 37 (2007) 414-437.
- 500 [56] E.P. Barrett, L.G. Joyner, P.P. Halenda, The Determination of Pore Volume and Area Distributions in Porous Substances. I.
501 Computations from Nitrogen Isotherms, *Journal of the American Chemical Society*, 73 (1951) 373-380.
- 502 [57] L.G. Joyner, E.P. Barrett, R. Skold, The Determination of Pore Volume and Area Distributions in Porous Substances. II. Comparison
503 between Nitrogen Isotherm and Mercury Porosimeter Methods, *Journal of the American Chemical Society*, 73 (1951) 3155-3158.
- 504 [58] S.L. Teich-McGoldrick, J.A. Greathouse, C.F. Jové-Colón, R.T. Cygan, Swelling Properties of Montmorillonite and Beidellite Clay
505 Minerals from Molecular Simulation: Comparison of Temperature, Interlayer Cation, and Charge Location Effects, *The Journal of Physical*
506 *Chemistry C*, 119 (2015) 20880-20891.
- 507 [59] H. Suquet, C. de la Calle, H. Pezerat, Swelling and structural organization of saponite, *Clays and Clay Minerals*, 23 (1975) 1-9.
- 508 [60] M.F. Brigatti, L. Poppi, Natural and monoionic alietite; hydration and dehydration states, *Clay Minerals*, 22 (1987) 187-197.
- 509 [61] J. Cases, I. Bérend, M. François, J. Uriot, L. Michot, F. Thomas, Mechanism of adsorption and desorption of water vapor by homoionic
510 montmorillonite; 3, The Mg (super 2+), Ca (super 2+), and Ba (super 3+) exchanged forms, *Clays and Clay Minerals*, 45 (1997) 8-22.
- 511 [62] J. Cases, I. Bérend, G. Besson, M. Francois, J. Uriot, F. Thomas, J. Poirier, Mechanism of adsorption and desorption of water vapor by
512 homoionic montmorillonite. 1. The sodium-exchanged form, *Langmuir*, 8 (1992) 2730-2739.
- 513 [63] I. Berend, J.-M. Cases, M. Francois, J.-P. Uriot, L. Michot, A. Masion, F. Thomas, Mechanism of adsorption and desorption of water
514 vapor by homoionic montmorillonites; 2, The Li (super +) , Na (super +) , K (super +) , Rb (super +) and Cs (super +) -exchanged forms,
515 *Clays and Clay Minerals*, 43 (1995) 324-336.
- 516 [64] E.M. Gartner, I. Maruyama, J.J. Chen, A kinetic explanation for the composition and physico-chemical behaviour of C-S-H formed
517 during the hydration of Portland cements., (submitted to CCR).